

SMALL-SCALE MECHANICAL PROPERTIES OF ADDITIVELY MANUFACTURED Ti-6Al-4V

M. Haghshenas^{1,*}, O. Totuk², M. Masoomi³, S.M. Thompson³, N. Shamsaei³

¹ Department of Mechanical Engineering, University of North Dakota, Grand Forks, USA

² Department of Mechanical Engineering, Cankaya University, Ankara, Turkey

³ Laboratory for Fatigue & Additive Manufacturing Excellence, Auburn University, Auburn, USA

Abstract

This article aims at studying microstructure and nano/micro-scale mechanical responses of Ti-6Al-4V fabricated using a Laser-based Powder Bed Fusion (L-PBF) method. To this end, an instrumented depth-sensing nanoindentation system has been used to assess hardness, Young's modulus, strain rate sensitivity and rate dependent plastic deformation of the alloy at different build Orientations (in the *Z*-plane and *X*-plane) at ambient temperature. Indentation tests were conducted at constant proportional loading rate of 15 mN/s in a depth-controlled ($h_{ind}=2000$ nm) testing regime. The Microstructure characterizations were performed using optical and scanning electron microscopy to assess the correlations to the mechanical properties achieved by the nanoindentation testing to better establish structure-property relationships for L-PBF Ti-6Al-4V. It is expected that the fine microstructure, developed by fast solidification during the L-PBF process, to directly contribute to the nanoindentation measurements at different strain rates.

Keywords: Ti-6Al-4V; additive manufacturing; mechanical properties; nanoindentation; microstructure.

* Corresponding author (Meysam Haghshenas)

Email: meysam.haghshenas@engr.und.edu

1. Introduction

Ti-6Al-4V, an α (*hcp*)/ β (*bcc*) titanium (Ti), is the most widely used Ti alloy which account for more than half of all commercial Ti applications [1]. 80% of the produced Ti-6Al-4V is used in aerospace applications and the rest is found in other applications including defense, marine, medical, chemical, and other industries [2]. However, this alloy is not necessarily a friendly one with respect to conventional manufacturing processes such as welding, forming, casting and machining. Additive manufacturing (AM), a rapidly growing net (or near net) shape manufacturing operation, seems an ideal replacement for the conventional manufacturing of the Ti-6Al-4V alloy thanks to its numerous advantages over traditional methods of manufacturing, such as energy savings, decreased material waste, shorter design-to-final fabrication time, and enhanced material properties. However, the thermal processing history (*i.e.* rapid cooling rate) of the alloy during AM process, is completely deferent with the one in other conventional manufacturing processes (*i.e.* casting) and this results in anisotropy (consisting of large prior β grains) in the microstructure of additively manufactured Ti-6Al-4V alloys. Therefore, it seems essential to assess properties/processing/structure correlation of the additively manufactured materials (in this study Ti-6Al-4V) to understand their potential in meeting demanding service requirements.

Instrumented nanoindentation testing technique is a reliable, convenient, and in-situ experimental approach to assess local mechanical properties, *i.e.* at the sub-micron level, and rate-dependent plastic deformation of metals (*i.e.* creep) in the nanoscale. During a typical nanoindentation test, indenter load (micro-milli Newton rang) and displacement (nanometer-micrometer range) are recorded as the indenter tip is pressed into the test material. Tests can be done either under load controlled (pre-set load) or depth controlled (pre-set depth). A wealth of mechanical and physical properties (hardness, indentation stress, indentation strain rate sensitivity, reduced modulus, indentation size effect, etc.) can be extracted from load-displacement (*P-h*) curves which are essentially different for diverse materials [3]. Also, this is a very powerful technique to study metallurgical phenomena such as dislocation activity, phase transformation, and shear localization in different metals and alloys. Since the deformation induced by an indenter during a nanoindentation test scheme is much localized in a very small zone underneath the indenter, the mentioned physical/metallurgical events show up as discrete variations in the *P-h* curve and therefore can be studied well in detail.

The effects of different thermal cycles in AM of the alloy on local mechanical properties (*i.e.* hardness distribution) can be well assessed through an instrumented nanoindentation testing method. Thanks to its unique capability, within last five years, researchers have shown great interests in using nanoindentation testing approach to assess different local properties in additively manufactured material [4-7]. Zhou *et al* [4] used nanoindentation testing to assess the mechanical properties of freeform bio-medical parts made by Additive Manufacturing (AM). They reported about 15% error when measuring Young's modulus at horizontal position while a larger error happens when measuring at an inclined position in their indentation testing data. They contributed this uncertainty to the large volume of porosity in the AM specimens. Everitt *et al* [5] and Aboulkhair *et al* [6] used nanoindentation to study the local mechanical properties of the selective laser melted (SLM) AlSi10Mg alloy. They reported uniform nano-hardness profile in the SLM melt pool and also across the surface of a whole layer. This was attributed to the extremely fine microstructure along with the good dispersion of the alloying elements. Gong *et al* [7] assessed nanoindentation characterization of Ti-6Al-4V parts made through electron beam additive manufacturing. They reported that the highest Young's modulus and hardness are located at the Z-plane of the top layers and the Young's modulus and hardness are higher on the Z-plane than those from the X-plane.

Upon a comprehensive literature review and to the best of our knowledge, it seems lack of systematic knowledge on nanoindentation-based experiments on AM of Ti-6Al-4V with respect to indentation size effect, rate-dependent deformation, and indentation strain rate sensitivity. These are required to assess rate-controlling indentation mechanisms versus indentation depth and to further analyze the contributing parameters in terms of dislocation activation energy and activation volume.

2. Experimental procedure

The starting material for this study is Ti-6Al-4V fabricated using a laser-based powder bed fusion (L-PBF) method. Using a 3D printing Machine Nd:YAG laser source ($\lambda=1.06 \mu\text{m}$) rectangular shaped specimens of 4 mm in thickness by 40 mm length and 10 mm width 6 mm were printed on a bi-directional 'zigzag' scanning pattern. Prior to microstructural and nanoindentation assessments, manufacture samples were sectioned, mechanically ground and polished using standard metallographic procedures. Samples separated for microstructural studies were etched

using Kroll's Reagen (92 mL distilled water, 6 mL nitric acid, 2 mL hydrofluoric acid) were examined using an MTI Advanced Metallurgical Microscope.

Nanoindentation tests in this study were performed on a NanoTest Vantage system designed and manufactured by Micro Materials Ltd. (Wrexham, UK). NanoTest Vantage system works by measuring the indentation force and the indenter motion when it is in contact with the test material. The sequence begins by applying an increasing amount of force to the indenter to indent a polished sample to a predetermined force/depth at a defined loading rate. The indentation force, depth and time data are recorded by the NanoTest software. To run an accurate indentation test, a number of test calibrations, of which the two most important are the load and depth calibrations, were performed.

A geometrically self-similar three-sided pyramid Berkovich indenter was used for the nanoindentation tests; this is the most commonly used indenter in acquiring the nanomechanical data. The tests were performed at constant temperature of 20°C under a constant load rate regime (15 mN/sec) in a depth controlled mode to a maximum depth of 2000 nm at different areas of the printed specimen (*i.e.* top, bottom middle, see Fig. 1). Distance between the indentations was set as 100 µm. During each test the indentation depth, corrected for both thermal drift and elastic compliance of the test frame, was recorded at intervals of 100 msec. During unloading, at 10% of the peak load a holding time of 120 s is provided to the machine to account for possible thermal drift correction (thermal drift was kept below 0.05 nm/s).

In the current work, Oliver-Pharr analysis [8] was used to assess indentation hardness and reduced elastic modulus of the samples with the reduced elastic modulus (E_r) calculated from the unloading curves. In Oliver and Pharr's nanoindentation model [8], the projected contact area of the indentation, A_c , is defined by a polynomial function as:

$$A_c = \sum_{n=0}^8 C_n h_c^{\frac{1}{2n-1}} \quad (1)$$

where h_c is contact depth, which can be expressed by:

$$h_c = h_{\max} - \varepsilon \frac{P_{\max}}{S} \quad (2)$$

where P_{max} is the peak load, h_{max} is the displacement at the maximum load, ε is a constant equal to 0.75 and S is the contact stiffness, $\frac{dP}{dh}$, (see Fig. 1). By having indentation load and A_c , one can easily calculate indentation hardness as:

$$H_{ind} = P / A_c \quad (3)$$

The reduced elastic modulus, E_r , for the specimen/indenter system can be calculated using the equation:

$$\frac{1}{E_r} = \frac{(1-\nu_s^2)}{E_s} + \frac{(1-\nu_i^2)}{E_i} \quad (4)$$

where E_s and E_i are Young's moduli, and ν_s and ν_i are Poisson's ratios, for the specimen and for the indenter tip, respectively.

The relationship between the load–displacement data and the experimentally measured contact stiffness (S) and the contact area (A) is

$$E_r = \frac{S\sqrt{\pi}}{2\sqrt{A}} \quad (5)$$

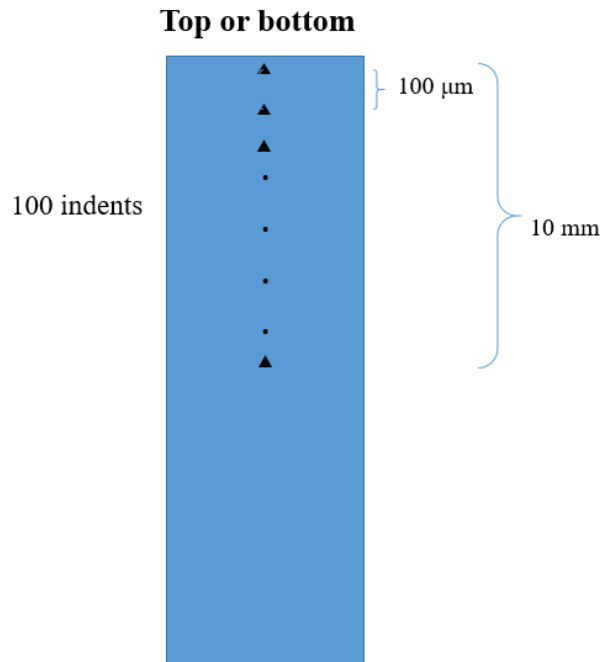


Figure 1: indentation scheme used in this study.

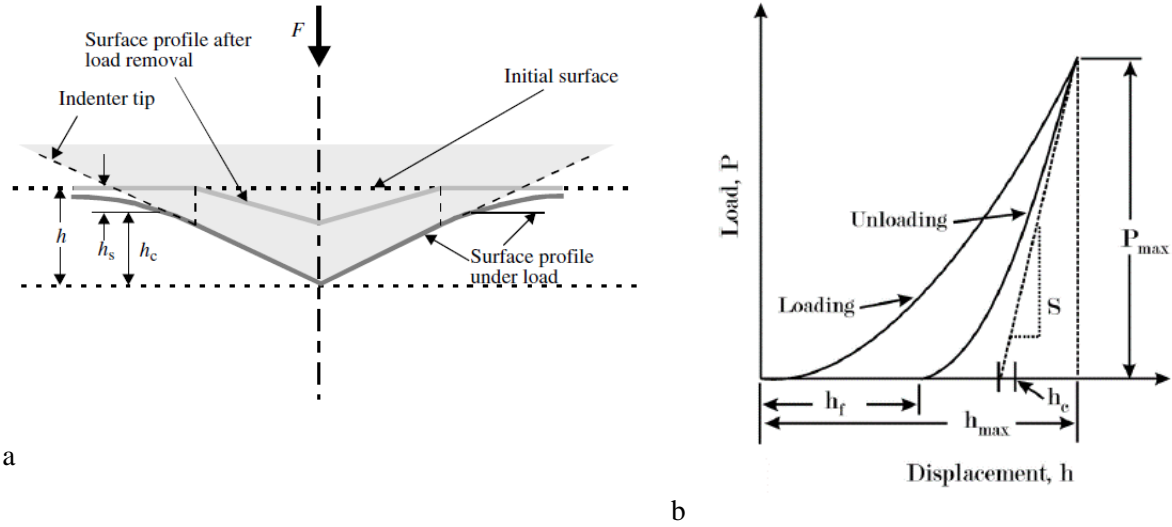


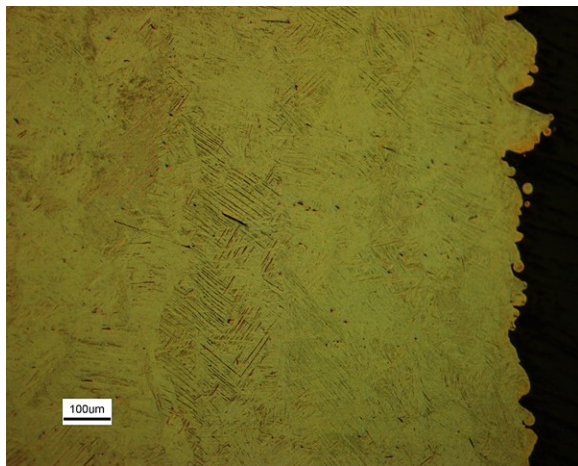
Figure 2: Schematic representation of a section through an indentation, showing various quantities used in the analysis (Oliver and Pharr, 1992 [8]): F , indentation load; h , indenter displacement at peak load; h_c , contact depth; h_s , elastic deformation of the surface at the contact perimeter [9].

3. Results and discussion

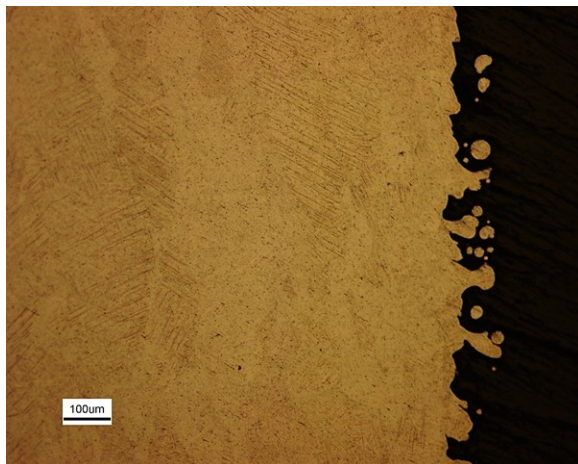
3.1. Microstructure

In the L-PBF process, the rate of cooling varies at different locations, bottom (close to the substrate), middle, and top end of the deposit. That is, a strong thermal gradient exists in the build direction in the additive manufacturing operations including L-PBF process. Therefore, depending on the distance of the deposited layers from the substrate, different solidification patterns (structure) are developed in the specimen. This can be mimicked with a Jominy end quench testing set-up in which quenching from one end results in different microstructures and therefore diverse mechanical properties at different distances from the quench end. At the start of deposition, the base plate acts as a quench media and extract heat from the very first layer rapidly. The rate at which solidification proceeds depends on heat transfer and thermal properties of the material being deposited. Because of the chilling action of the substrate, grain grow in a direction away from the heat transfer. This effect becomes less pronounced upon progression of layers' stacking which results in a continuous decreasing trend in the cooling rate toward top of the printed part away from the base substrate. This causes different microstructures (*i.e.* fine equiaxed, dendritic, coarse equiaxed) corresponding to different mechanical responses (*i.e.* hardness readings).

In the Ti-6Al-4V alloy, low to intermediate cooling rates create an α - β lamellar structure with α -phase lamellae in a β -phase matrix. The formation of α -lamellae is a diffusion controlled nucleation and growth mechanism of the α -lamellae into the β -grains. As cooling rates increase the length and thickness of the α -lamellae decrease which leads to higher yield strengths. A common α - β microstructure with α -lamellae shows the finer α -lamellae and how cooling rate affects the structure of the phases in the resultant microstructures. With increased cooling rates the α -lamellae's thickness and length decreases. Since parts cool faster towards the outside of the part (top and bottom zones in the additively manufactured alloy), due to diffusion of heat through the part, it is expected that towards the center of the part the α -lamellae should be thicker and longer since cooling will occur slower. Figure 2 shows the microstructure in the top, middle, and bottom of the deposit which includes columnar prior β grains along with α at grain boundaries. The columnar structure is a typical feature in the AM.



a



b



c

Figure 1: Optical microscopy images in the a) top, b) bottom, c) middle.

3.2. Nanoindentation response

Fig. 3 shows indentation hardness versus indentation depth at 15 mN/min loading rate. With decreasing indentation depth, indentation hardness increases (shallow indentations result in higher hardness for geometrically self-similar indenters such as Berkovich indenter used in this study) which contradicts conventional plasticity behavior (in classical continuum plasticity models, the stress-strain responses are size independent (Fig. 4)). This is a clear indication of indentation size effect (ISE). Generally, the ISE phenomenon shows up due to the following reasons [10-15]:

- High strain gradients at shallow indentation depths due to the presence of geometrically necessary dislocation (GNDs). Density of GNDs is in inverse relation with indenter displacement, h . For small indentation depths, some kind of dislocations, *i.e.* GNDs, are required to accommodate for the lattice curvature imposed by lateral side of the penetrating self-similar, *i.e.* Berkovich, indenter. Since GNDs are forced to nucleate and glide in a very small volume of material just underneath the indenter, which may not contain easy slip systems, they may act as glide-limited obstacles to other mobile dislocations. This results in the increased applied stresses necessary for dislocation to glide and eventually increase in the hardness (indentation stress) at sub-micron depths.
- Dislocation starvation: In nanometer scale indentations, where crystal being dislocation starved and requiring the nucleation of dislocations to initiate plasticity, ISE is attributed to the dislocation starvation mechanism. That is, beneath the indenter, due to the small volume of material, may contain literally no easy dislocation nucleation sources and

reaches the starvation state. Therefore, further plastic deformation requires the increase of external applied indentation load to initiate the nucleation of new dislocations.

- Surface artifacts and sample preparation (surface topography, hardened surface layers due to polishing, oxidation, indenter blunting, sink-in/pile-up around indentation,). All these surface related artifacts (*i*) create significant scatter and error in shallow indentation data, (*ii*) contribute directly to ISE. For instance, in mechanical polishing, the surface (and subsurface) material is work hardened which becomes increasingly saturated with new dislocations; this in turn increases the hardness and strength by the Taylor mechanism in for the shallow indentations.

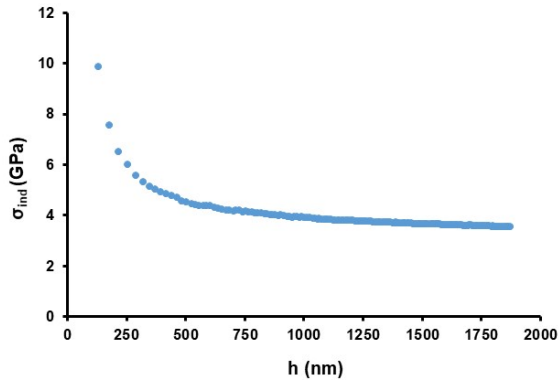


Figure 3: Indentation stress versus indentation depth.

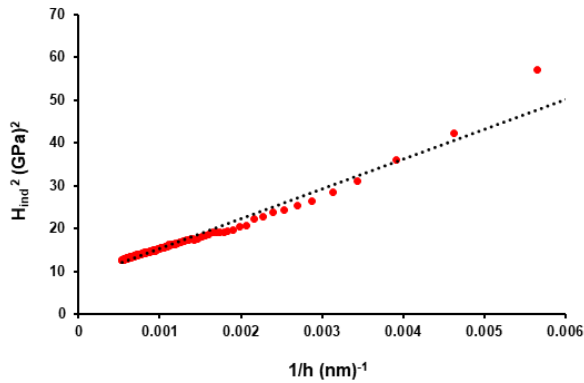


Figure 4: Indentation hardness, squared, versus inverse of indentation depth.

To characterize the ISE of hardness, Nix and Gao [15] developed a GND-based model as:

$$\left(\frac{H_{ind}}{H_0}\right)^2 = 1 + \frac{h^*}{h} \quad (7)$$

By rearranging Eq. 7 one can write:

$$H_{ind}^2 = H_0^2 + h^* H_0^2 \left(\frac{1}{h}\right) \quad (8)$$

where h is the indentation depth, H_0 is the indentation hardness for a large indentation depth, and h^* is a characteristic length that depends on the properties of indented material and the indenter angle. The H_0 can be expressed as:

$$H_0 = 3\sqrt{3}\alpha Gb\sqrt{\rho_s} \quad (9)$$

where α is the geometric constant, G is the shear modulus, b is the Burger vector and ρ_s stands for density of statistically stored dislocations (SSDs). It has been reported that this equation overestimates the hardness value for the very small indentation depths (*i.e.* 100 to 200 nm) and this has been attributed to very large density of GNDs at shallow depths [38]. Figure 10 shows curves of H_{ind}^2 versus inverse of indentation depth, $\frac{1}{h}$, at different indentation strain rates. As seen, a single linear trend cannot be fitted to each graph at each strain rate meaning that Nix-Gao model does not hold for shallow indentation depths (it deviates from a linear trend with decreasing indentation depth).

Figure 5 shows the plots of indentation load versus depth on the Z-direction from the bottom part for all 100 indents. The calculated average reduced modulus is equal to 140 GPa which is in good agreement with the reported Young's modulus for the Ti-6Al-4V alloy in the literature [16-18]. The hardness was obtained as the ratio of the maximum indentation force to the resultant projected contact area evaluated from the shape function of the indenter and the maximum indent displacement. The average calculated hardness of this sample is 4.48 GPa.

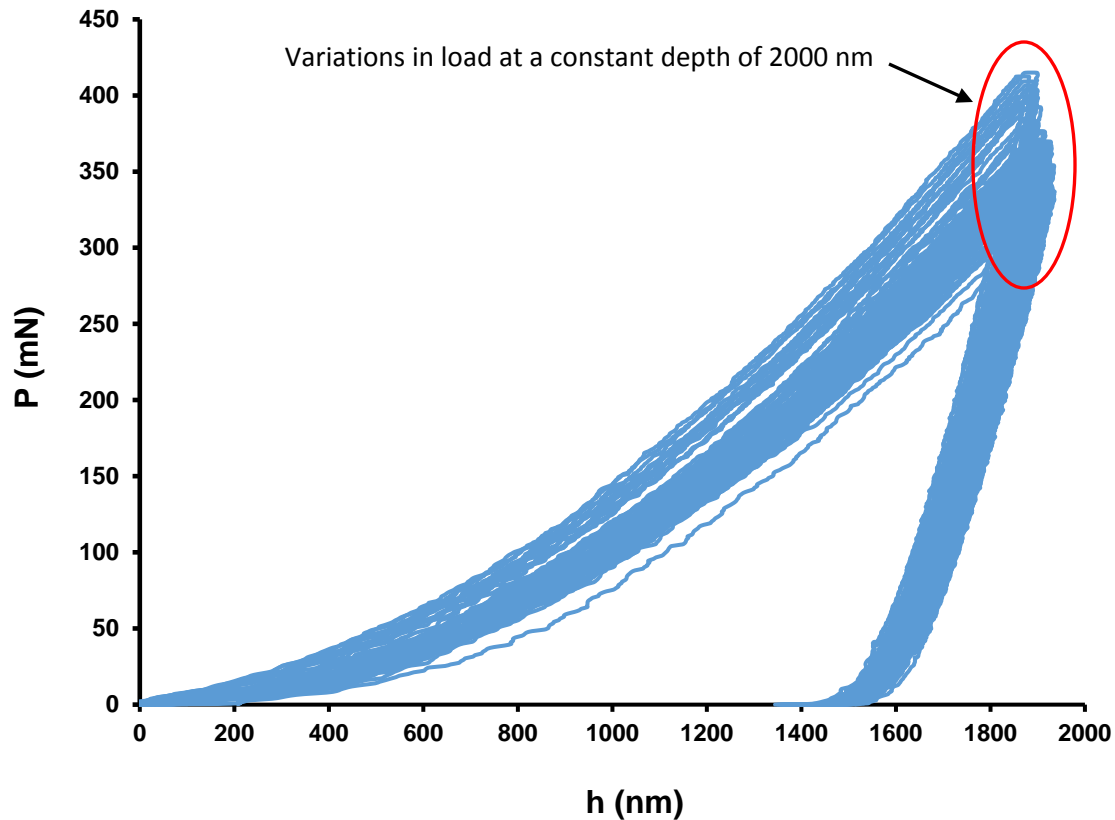


Figure 5: the plots of indentation load versus depth on the Z-direction from the bottom part for all 100 indents. Clear variations in the indentation load, at a constant depth of 2000 nm, are observed which shows different local properties at different positions on the sample.

The microstructure and the local mechanical properties, like hardness distribution, are affected by repeated thermal cycles that occur during the deposition process. Having said this, it is expected to have the highest hardness and Young's modulus for the top layers where there are less repeated thermal cycles. However, in the middle layers, the microstructure is much coarser because of more exposure to the heating/reheating cycles. In the bottom part, the base plate and deposited material act as a heat sink during deposition which results in higher cooling rate and finer microstructure. This, based on Hall-Petch rule results in higher strength (hardness).

Figure 6 shows the variation of hardness and reduced modulus for bottom and top layers. As seen, larger H and E_r are recorded with approaching to the very bottom layers. Also, large scatters are observed in H and E_r for the "Top" layers. This might be attributed to larger density of defects, non-uniform cooling gradient, and partially consolidated particles toward the top of the printed specimen.

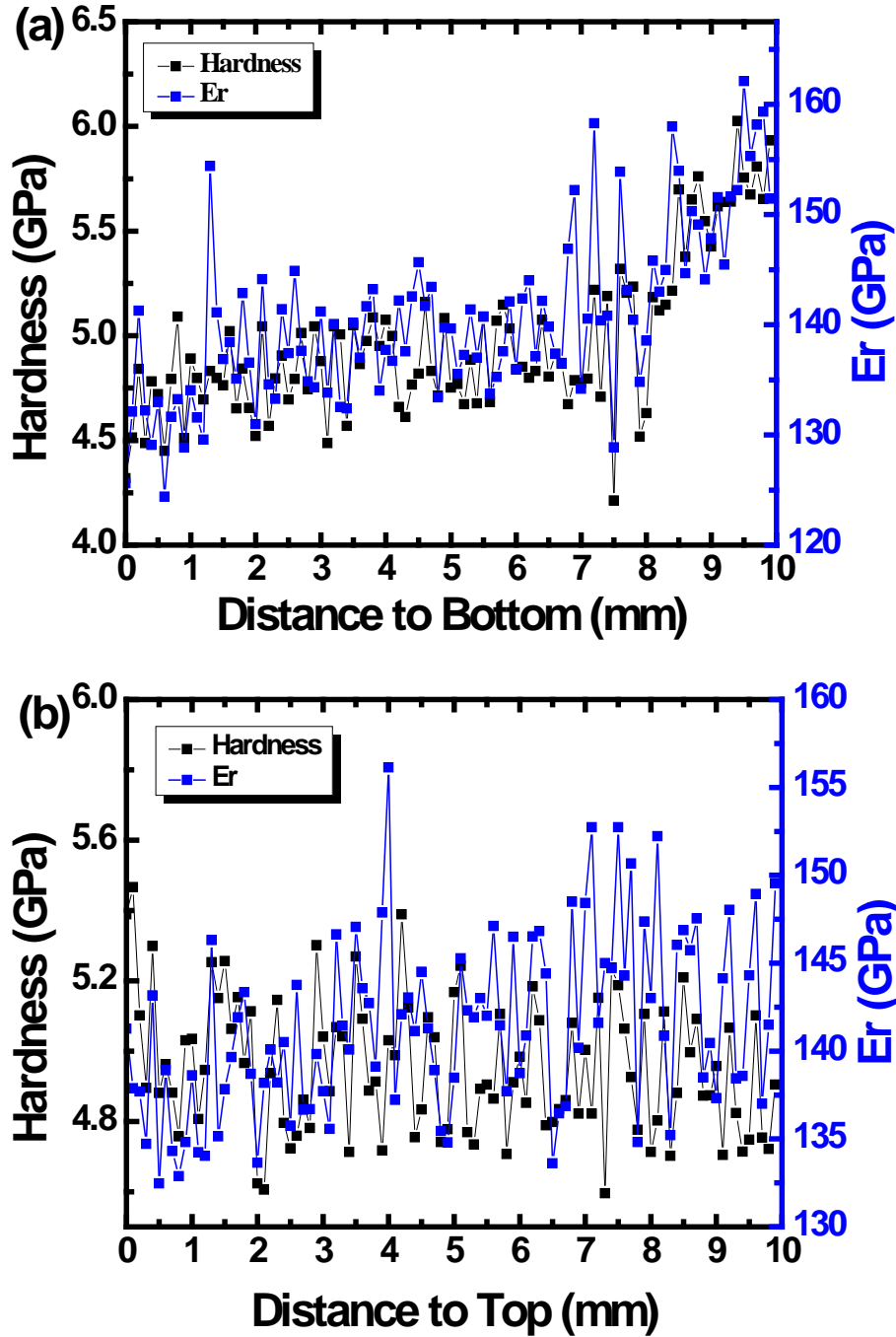


Figure 6: Variation of hardness and reduced modulus for a) bottom zone, b) top zone.

Conclusions

In the present study, through a nanoindentation approach, local mechanical properties of an additively manufactured Ti-6Al-4V alloy were studied to establish the relationship between local hardness and the microstructure.

- The microstructure of AM Ti-6Al-4V varies along the build direction (*i.e.* top, middle, and bottom); this is because of different cooling rate at different positions. The middle layers are necessarily thicker and wider because of slow cooling rate.
- A clear indentation size effect (ISE) response was observed in the hardness (indentation stress) *versus* depth graphs. This phenomenon is attributed to the GNDs, dislocation starvation mechanism and surface artifacts.
- The calculated average reduced modulus is equal to 140 GPa which is in good agreement with the reported Young's modulus for the Ti-6Al-4V alloy in the literature
- Strength of the material (*i.e.* indentation hardness) varies along the build direction. This is because of different cooling rate that results in different microstructure and therefore diverse mechanical properties (Hall-Petch relation).

Reference

1. M. Peters, C. Leyens, Titanium and titanium alloys, Weinheim, Wiley-VCH (2003) page 513.
2. Scott Mitzner, Stephen Liu, Marcia Domack, Robert Hafley, 26th Annual International Solid Freeform Fabrication Symposium, At Austin, Texas, USA.
3. Christopher A. Schuh, Materials Today 9 (2006) 32-40.
4. Yuhaowei Zhou, Yunlong Tang, Thibault Hoff, Martin Garon, Fiona Yaoyao Zhao, Procedia Manufacturing 1 (2015) 327–342, 43rd Proceedings of the North American Manufacturing Research.
5. Nicola M. Everitt, Nesma T. Aboulkhair, Ian Maskery, Chris J. Tuck, Ian Ashcroft, Advanced Materials Letters 71 (2016) 13-16.
6. Nesma T. Aboulkhair, Alex Stephens, Ian Maskery, Chris Tuck, Ian Ashcroft, Nicola M. Everitt, 26th Annual International Solid Freeform Fabrication Symposium, At Austin, Texas, USA.
7. Xibing Gong, James Lydon, Kenneth Cooper, Kevin Chou, Proceedings of the ASME 2014 International Mechanical Engineering Congress and Exposition IMECE2014, November 14-20, 2014, Montreal, Quebec, Canada.
8. W.C. Oliver, G.M. Pharr, Journal of Materials Research 7 (1992) 1564- 1583.
9. N. Barbakadze, S. Enders, S. Gorb, E. Arzt, The Journal of Experimental Biology 209 (2006) 722-730.
10. Julia R. Greer, William D. Nix, PHYSICAL REVIEW B 73, 245410 (2006)
11. William D. Nix, Julia R. Greer, Gang Feng, Erica T. Lilleodden, Thin Solid Films 515 (2007) 3152–3157.

12. W. W. Gerberich, N. I. Tymiak, J. C. Grunlan, M. F. Horstemeyer, I. Baskes, *Journal of Applied Mechanics* 69 (2002) 433-442.
13. Ilze Manika, Janis Maniks, *Acta Materialia* 54 (2006) 2049–2056.
14. George M. Pharr, Erik G. Herbert, Yanfei Gao, *Annual Reviews, Mater. Res.* 40 (2010) 271–292.
15. Nix, W.D., Gao, H., *J. Mech. Phys. Solids* 46 (1998) 411–425.
16. Xue, W., Wang, C., Chen, R., and Deng, Z., *Materials Letter* 52 (2012) 435-441.
17. Barbieri, F.C., Otani, C., Lepienski, C.M., Urruchi, W.I., Maciel, H.S., Petraconi, G, *Vacuum* 67 (2002) 457-461.
18. Xibing Gong, James Lydon, Kenneth Cooper, Kevin Chou, *Proceedings of the ASME 2014 International Mechanical Engineering Congress and Exposition, IMECE2014*, November 14-20, 2014, Montreal, Quebec, Canada.